IEEE Photonics Journal
An IEEE Photonics Society Publication

Dual-Bandwidth Linear Polarization Converter Based on Anisotropic Metasurface

Volume 12, Number 2, April 2020

Changfeng Fu
Zhijie Sun
Lianfu Han
Chao Liu

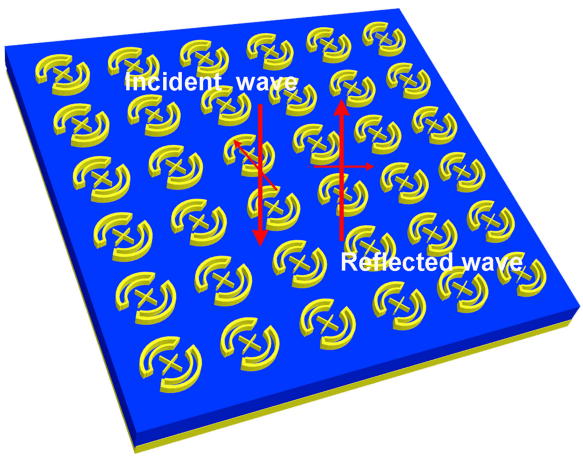

DOI: 10.1109/JPHOT.2019.2962336

Dual-Bandwidth Linear Polarization Converter Based on Anisotropic Metasurface

Changfeng Fu,[1,2] Zhijie Sun ,[1] Lianfu Han,[2] and Chao Liu[2]

[1]Institute of Materials Processing and Intelligent Manufacturing, College of Materials Science and Chemical Engineering, Harbin Engineering University, Harbin 150001, P.R. China
[2]School of Electronics Science, Northeast Petroleum University, Daqing 163318, P.R. China

DOI:10.1109/JPHOT.2019.2962336

Manuscript received September 12, 2019; revised December 18, 2019; accepted December 20, 2019. Date of publication January 1, 2020; date of current version March 26, 2020. This work was supported in part by the Natural Science Foundation of China under Grant 51774092, in part by the Youth Science Foundation of Northeast Petroleum University of China under Grant 2018QNL-39, and in part by the Postdoctoral Science Foundation of China under Grant 2016M601400. Corresponding author: Zhijie Sun (e-mail: zhijiesun@hrbeu.edu.cn).

Abstract: In this work, a metasurface with the symmetrical double C-shaped narrow ring connected with the central cross structure is investigated by simulation, theory and experiment, which can near-perfectly convert linearly polarized electromagnetic waves into their orthogonal components in the frequency ranges from 9.38 to 13.36 GHz and 14.84 to 20.36 GHz. And the corresponding fractional bandwidths within the two bands are 35.00% and 31.36%, respectively. The influences of structural parameters on the polarization conversion performance are studied. The results show that the central frequencies and bandwidths of the two bands can be easily modulated by varying the structural parameters of r and θ. The high-efficiency and dual-broadband characteristics can also be well maintained in the oblique incidence range of 0–45°. Meanwhile, the mechanisms of polarization conversion are analysed, and several formulas are used to calculate the reflection coefficients of the co- and cross-polarization under the normal incident *y*-polarized electromagnetic waves based on the phase difference of the reflection coefficients of the *u*- and *v*-polarized conversions. The experiment results are in good agreement with those of simulations and theoretical analysis. The proposed metasurface has important applications in novel polarization control devices.

Index Terms: Anisotropic metasurface, polarization conversion, dual-wideband, high-efficiency.

1. Introduction

Metasurface is a sort of artificial two-dimensional material containing periodic or aperiodic sub-wavelength units, possessing unique characteristics of manipulating electromagnetic (EM) waves [1]–[5]. Compared with traditional metamaterial, metasurface has advantages of low loss, low profile and easy processing [6], [7]. Recently, artificial metasurface structures have been extensively used to manipulate EM waves, particularly in control polarization [8]–[12]. Metasurface provides an encouraging method for polarization control because it can make the EM amplitude and phase of scattered light change abruptly within the sub-wavelength space region [13]–[18].

Numerous reflective and transmissive polarization converters based upon chiral or anisotropic metasurfaces have been designed from microwave to optical frequencies [19]–[25]. For example, Hao *et al.* [26] designed a linear polarization converter using anisotropic metamaterial with I-shaped structure. However, there exists an obvious shortcoming of narrow bandwidth. Subsequently, a variety of methods such as small-scale design [27], multi-layer [28] and multi-resonance design [29], [30] have been introduced to improve the polarization conversion bandwidth. Lin *et al.* proposed a wideband polarization converter with multilayered structure to achieve linear-to-circular polarization conversion from 12.21 to 18.39 GHz [31]. Grady *et al.* described a broadband ultrathin metamaterial with a multilayered structure for linear polarization conversion in the range of 0.52 to 1.82 THz [32]. Although great advances have been made in polarization conversion bandwidth, low efficiency is a serious obstacle hindering potential applications. Therefore, many efforts are required for structure designs of metasurface with high efficiency, broadband and easy-to-manufacture cell structure. In particular, the total reflection coefficients closely related to polarization converter need to be further explored and explained.

Herein, a perfect and dual-broadband linear polarization converter is theoretically proposed and experimentally demonstrated. The converter consists of the symmetrical double C-shaped narrow ring connected with the central cross structure, a dielectric layer and a metal plate. Four resonances occur within the 9.38–13.36 GHz and 14.84–20.36 GHz frequency ranges. In these dual-band ranges, *x*-polarized or *y*-polarized incident waves can almost be completely converted into corresponding cross-polarized waves. The polarization conversion ratios (PCR) for the dual bands are more than 98.21% and 99.32%, respectively. The physical mechanisms of polarization converter are discussed in detail. In addition, the high-efficiency and dual-broadband characteristics can be maintained when the incident angle increases to 45°. The proposed metasurface has advantages of simple geometric structure, high efficiency and wide bandwidth comparing with the previous designs [33], [34], hence exhibiting great application potential in polarization control devices.

2. Metasurface Design and Experiment

The proposed reflective polarization converter with dual band consists of three layers sandwiched structure, including the bottom full metallic layer, the intermediate dielectric layer, and the top electric resonator structure. To generate the orthotropic wave for the *x*- or *y*-polarization incident wave, the electric resonator structure should be asymmetrical about *x*- and *y*-axis. However, the electric resonator structure should also have a symmetric axis marked by *u*(*v*)-axis along 45° direction respect to *x*- or *y*-axis, so that the 90° polarization conversion can be achieved when the *x*- or *y*-polarized waves illuminate the metasurface structure.

Based on the above design guidelines, we propose a metasurface structure with reflective polarization conversion as shown in Fig. 1. The unit cell is composed of three layers, and the symmetrical double C-shaped narrow ring connected with the central cross structure on the top level. The intermediate layer is F4B ($\varepsilon_r = 2.65 - 0.001\,j$) with a thickness d of 3 mm. The bottom layer is an all-metal plate. Two metal parts are formed by copper films with electrical conductivity of 5.8×10^7 S/m and thickness of 35 μm. The optimized geometric parameters are listed in Table 1. To understand the principle of multiple resonances, we model the structure as an anisotropic structure with two symmetrical axes, *u*- and *v*-axes, as shown in Fig. 1(b). Under normal incidence, it is possible for the central cross structure to excite individual resonances by selecting the polarization angle of the incident linear polarization wave to be 0° or 90° relative to the *u*-axis. For the intermediate angles, both resonances are excited, so multiple resonances can be excited by properly selecting the incident polarization angle and the length of cross arm. On the other hand, the ring structure is a highly adjustable, which supports multipole modes excited by delay effects, oblique incidence or coupling with other structures, hence exciting the multiple resonances. The ring structure can adjust the bandwidth of the low frequency band and the high frequency band, so the center cross structure has a great influence on the high

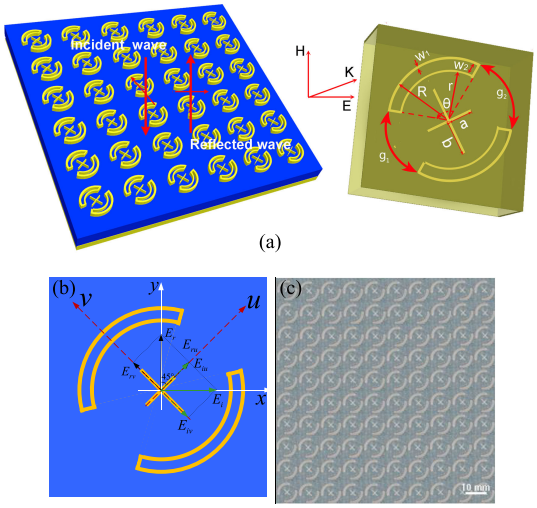

Fig. 1. (a) Schematic diagram of the unit cell structure and polarization converter under linear polarized light incidence, (b) definitions of the *u*- and *v*-axes (front view), (c) photograph of the prepared sample.

TABLE 1
Optimized Parameters of Metasurface Polarization Converter (mm)

p	a	b	w_1	w_2	R	r	ϑ	g_1	g_2
10	1	1.5	0.19	0.44	4.32	3.5	110°	5.28	5.28

band. The frequency ratio of dual-operation frequency can be realized by changing the structural parameters.

The design, simulation and optimization of the proposed converter are carried out by Comsol Multiphysics based on finite element method (FEM). The periodic boundary conditions are used in the *x* and *y* directions in the simulation. Because of geometric symmetry, the cross- and co-polarization reflection coefficients of *y*-polarized incident waves are similar to those of *x*-polarized incident waves. Consequently, the reflection coefficients of *y*-polarized incident wave are discussed. In addition, the wave vector $\vec{k}$ is negative along the *z* axis. The experiments are used to verify the polarization conversion behavior of the prepared samples. The sample with 10×10 mm^2 unit cells is prepared by the printed circuit board (PCB) technology. Fig. 1(c) shows the photograph of the prepared sample. An Agilent N5230A network analyzer and two of the same linear polarization standard gain horn antennas are applied to measure the cross- and co-polarization reflection coefficients of the samples in the anechoic chamber. Horn antenna 1 is fastened by horizontal polarization to transmit *y*-polarized incoming waves. Then *y*-polarized incoming waves will be reflected by the metasurface. Horn antenna 2 is put in the direction of vertical and horizontal polarization respectively in order to obtain reflection coefficients which are composed of cross- and co-polarized components.

3. Results and Discussion

3.1 Experiment and Simulation Results

The reflection coefficients of the co-polarization $r_{yy} = |E_{yr}/E_{yi}|$ and the cross-polarization $r_{xy} = |E_{xr}/E_{yi}|$ under the *y*-polarized incidence are used to better understand the polarization conversion

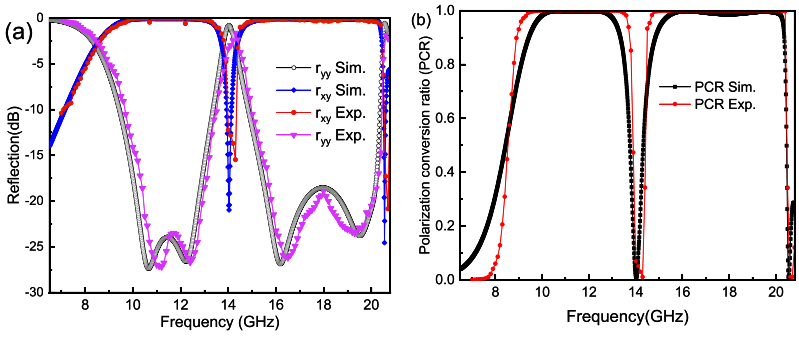

Fig. 2. Results of the simulation and experiment for *y*-polarized incidence, (a) cross- and co-polarized reflectance coefficients (r_{yy} and r_{yy}), (b) polarization conversion ratio (PCR).

response of the designed polarization converter. The subscript *x* and *y* signify the polarization direction of EM wave, respectively. And the subscript *i* and *r* denote the incident and reflected waves, respectively. PCR is described for characterizing the performance of polarization converters, and it is expressed as:

$$PCR = {r_{xy}}^2 / \left({r_{xy}}^2 + {r_{yy}}^2\right) \tag{1}$$

Fig. 2 shows the simulation and experiment results of the cross- and co-polarized reflection coefficients as well as PCR for *y*-polarized incidence in the frequency range from 6.5 to 20.8 GHz. It is seen from Fig. 2(a) that the simulated co-polarized reflectance of r_{yy} is less than -10 dB over the frequency ranges of 9.38–13.36 GHz and 14.84–20.36 GHz, while the simulated cross-polarized reflectance of r_{xy} is greater than -1 dB in the corresponding frequency ranges. The experiment results indicate that the measured r_{yy} is below -10 dB in the frequency ranges from 9.67 to 13.47 GHz and 14.96 to 20.45 GHz, whereas r_{xy} is more than -1dB in the same frequency ranges. Therefore, the designed polarization converter has the characteristics of dual-band. According to the simulation results, the four resonant frequencies are located at 10.67, 12.22, 16.18 and 19.51 GHz within the two frequency bands. The experiment results show that there are also four resonant frequencies locating at 11.16, 12.41, 16.49 and 19.26 GHz in two frequency bands. The simulation results in Fig. 2(b) indicate that the PCR is almost 98.21% within the frequency range 9.38 to 13.36 GHz. That is, on the bandwidth of 3.98 GHz, it is about 35.00% compared with the central frequency of 11.37 GHz. In the second frequency band (14.84–20.36 GHz), the PCR is higher than 99.32%, and the bandwidth is 5.29 GHz. The center frequency is situated at 17.61 GHz and the relative bandwidth of 31.36% is also obtained.

Furthermore, the corresponding frequencies of PCR almost closing to 1 are the same as those of the four frequencies with the minimum co-polarization reflection coefficient, as illustrated in Fig. 2. The experiment results are highly consistent with the simulation results, demonstrating that the *y*-polarized incident waves are almost converted into *x*-polarized reflected waves in the two frequency bands. However, there is a slight difference between simulation and experiment results, which is mainly attributed to the following two reasons. Firstly, periodic boundary conditions are adopted in the simulation and the structures along the *x*- and *y*-directions are considered to be infinite, whereas the prepared samples have a finite size. Secondly, a perfect normally-incident EM wave is used in the simulation, while the device uses a quasi-plane wave which can not be realized in the experiments. Based on the analysis above, the designed metasurface linear polarization converter has good characteristics of dual-band and high-efficiency.

3.2 Polarization State Analysis

To better understand the polarization state of reflected waves, elliptical angle χ and polarization angle ψ are defined. Fig. 3(a) shows the polarized ellipsoid of incident wave reflected by polarization converter. According to Fig. 3(a), the formulas of χ and ψ within the frequency range studied

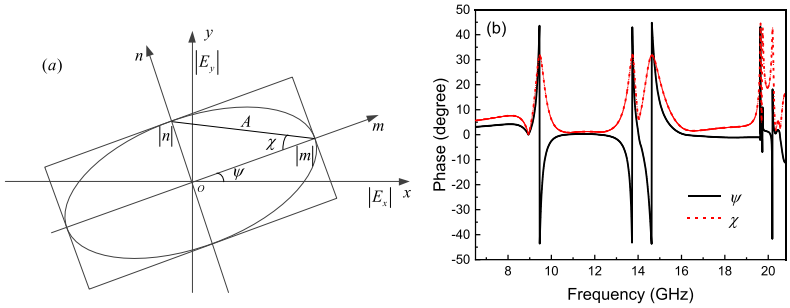

Fig. 3. (a) Polarized ellipsoid of incident wave reflected by polarization converter, (b) elliptical angle χ and polarization angle ψ of incident wave reflected by polarization converter.

are as follows [35], [36]:

$$\sin(2\chi) = \frac{2q_r \sin(\xi)}{1 + |q_r|^2} \tag{2}$$

$$\tan(2\psi) = \frac{2q_r \cos(\xi)}{1 - |q_r|^2} \tag{3}$$

$$\xi = Phase_{r_{xy}} - Phase_{r_{yy}} \tag{4}$$

where $q_r = |r_{xy}|/|r_{yy}|$ and ξ denotes the phase difference between r_{xy} and r_{yy}. The polarization angle $\psi \approx 0^\circ$ and the elliptical angle $\chi < 5^\circ$ at four resonant frequencies, illustrating that the reflected wave is approximately linear polarized wave perpendicular to the incident wave with relative high polarization purity, as shown in Fig. 3(b).

3.3 Theoretical Analysis

To study the mechanism of the dual broadband polarization converter, we define a pair of mutually perpendicular symmetry axis of the proposed metasurface by *u*- and *v*-axis. They have an angle of $\pm 45^\circ$ with the positive direction of *y*-axis, respectively, as shown in Fig. 1(b). Therefore, the designed structure can be considered as an anisotropic homogeneous metamaterial layer installed on a perfect metallic ground plate with a dispersive relative permeability tensor $\overleftrightarrow{\mu}$ and a relative permittivity ε_r. The $\overleftrightarrow{\mu}$ can be represented by diagonal elements μ_{uu}, μ_{vv} and μ_{zz} in the orthogonal coordinate system constituted of *u*-, *v*- and *z*- axis. Accordingly, there only consists of co-polarized components in the reflected waves when *u*- and *v*- polarization waves are illuminated. Supposing that the loss tangent of the dielectric layer can be neglected, the magnitude of reflections r_{uu} and r_{vv} would be both close to 1. However, the reflection phases($\Delta\phi_{uv}$) of r_{uu} and r_{vv} would have different owing to the anisotropic metasurface, so the polarization conversion of the reflection wave can be realized. Generally speaking, when the *y*-polarized wave is illuminated, $\Delta\phi_{uv} = 0^\circ$ means that there is no polarization conversion, that is, the reflected wave remains the y-polarized wave. When $\Delta\phi_{uv} = \pm\frac{\pi}{2}$, circular polarization conversion would be achieved. And if $\Delta\phi_{uv} = \pm\pi$, 90° linear polarization conversion would be achieved, that is to say, there is only *x* polarization in the reflected waves.

The analysis is also based on the normal incident y-polarized EM wave. In the direction of *u*- and *v*-axes, the electric field vectors of incident ($\vec{E}_i$) and reflected ($\vec{E}_r$) waves can be decomposed into two mutually perpendicular components with the same magnitudes, as depicted in Fig. 1(b). Their expressions are as follows:

$$\vec{E}_i = E_{yi}\vec{e}_y = E_{ui}\vec{e}_u + E_{vi}\vec{e}_v = \frac{\sqrt{2}}{2}E_{yi}\left(\vec{e}_u + \vec{e}_v\right) \tag{5}$$

$$\vec{E}_r = E_{xr}\vec{e}_x = E_{ur}\vec{e}_u + E_{vr}\vec{e}_v = r_u E_{ui}\vec{e}_u + r_v E_{vi}\vec{e}_v = \frac{\sqrt{2}}{2}E_{yi}\left(r_u\vec{e}_u + r_v\vec{e}_v\right) \tag{6}$$

where $\vec{e}_u$ and $\vec{e}_v$ denote the unit vectors in the direction of *u*- and *v*-axes directions, r_u and r_v represent the amplitudes of the reflection coefficients of the *u*- and *v*-polarized conversions, respectively. r_u and r_v are independent of each other, resulting from the anisotropy of structural element. Moreover, the value of the dielectric layer loss tangent is so small that it can be ignored. This leads to the magnitude of the co-polarized reflection coefficients of r_u and r_v closing to 1, while the cross-polarized reflection coefficients in *u*- and *v*-polarized directions are equal to zero.

$\Delta\phi_{uv} = \arg(r_u) - \arg(r_v)$ denotes the phase difference between r_u and r_v. Therefore, $\vec{E}_r$ can be described using the following expression:

$$\vec{E}_r = \frac{\sqrt{2}}{2} r_u E_{yi} \left(\vec{e}_u + e^{-j\Delta\phi_{uv}} \vec{e}_v \right) \tag{7}$$

Eq. (8) indicates that motion trajectory of reflected electric field vector $\vec{E}_r$ on any regular plane parallel to the *u*-*v* plane is perpendicular to the propagation direction. The above mentioned situation satisfies the following equation:

$$E_u{}^2 - 2E_v E_u \cos\Delta\phi_{uv} + E_v{}^2 = 0.5\left|E_{yi}\right|^2 \sin^2(\Delta\phi_{uv}) \tag{8}$$

As shown in Fig. 1(b), in the *x*-*y* frame of axes, using the equations $E_x = \frac{\sqrt{2}}{2} \cdot (E_u - E_v)$ and $E_y = \frac{\sqrt{2}}{2} \cdot (E_u + E_v)$, Eq. (8) can be expressed as:

$$\frac{2E_x{}^2}{\left|E_{yi}\right|^2(1 - \cos\Delta\phi_{uv})} + \frac{2E_y{}^2}{\left|E_{yi}\right|^2(1 + \cos\Delta\phi_{uv})} = 1 \tag{9}$$

Eq. (9) denotes the amplitudes of the *x*-polarization component and the *y*-polarization component in the reflected wave as follows:

$$\begin{cases} E_{xr} = |E_x|\,|_{E_y=0} = \frac{\sqrt{2}}{2}\left|E_{yi}\right| \sqrt{1 - \cos\Delta\phi_{uv}} \\ E_{yr} = \left|E_y\right|\,|_{E_x=0} = \frac{\sqrt{2}}{2}\left|E_{yi}\right| \sqrt{1 + \cos\Delta\phi_{uv}} \end{cases} \tag{10}$$

Therefore, reflection coefficients of the co-polarization (*y*-to-*y*) and the cross-polarization (*y*-to-*x*) can be defined as:

$$r_{yy} = \frac{\left|E_{yr}\right|}{\left|E_{yi}\right|} = \frac{\sqrt{2}}{2}\sqrt{1 + \cos\Delta\phi_{uv}} \tag{11}$$

$$r_{xy} = \frac{|E_{xr}|}{\left|E_{yi}\right|} = \frac{\sqrt{2}}{2}\sqrt{1 - \cos\Delta\phi_{uv}} \tag{12}$$

According to Eqs. (11) and (12), r_{yy} and r_{xy} are calculated on base of the value of $\Delta\phi_{uv}$.

In order to verify the performance of the designed linear polarization converter by Eqs. (11) and (12), numerical simulations are carried out under *u*- and *v*-polarized incoming, respectively. Fig. 4(a) shows that the simulation values of reflected amplitudes of the cross-polarization (r_{uv} and r_{vu}) are approximately zero and the co-polarization (r_{uu} and r_{vv}) are both close to unity over the frequency ranges of 9.38–13.36 GHz and 14.84–20.36 GHz, which demonstrates that there is no cross-polarized refection and the reflected EM wave can only be expressed using the same reflectance and phase in *u*- and *v*-polarized directions. Fig. 4(b) shows the phase and phase difference of the co-polarization in the *u*- and *v*-axis directions. In the first frequency band (9.38–13.36 GHz), the phase difference $\Delta\phi_{uv}$ is closed to $-180°$, while in the second frequency band (14.84–20.36 GHz), the phase difference $\Delta\phi_{uv}$ is to 180°. Moreover, $\Delta\phi_{uv}$ is exactly $-180°$ at the two frequencies of 10.67 and 12.23 GHz, respectively. $\Delta\phi_{uv}$ is just 180°, and the corresponding two frequencies are 16.19 and 19.67 GHz. These four frequencies are almost identical to the four resonance frequencies (10.67, 12.22, 16.18 and 19.51 GHz) in Fig. 2a. In addition, $\Delta\phi_{uv}$ is exactly equal to 0° at the frequency of 14.03 GHz, where is hardly any cross-polarized refection, as indicated in Fig. 2(b). The reflection coefficients of cross- and co-polarization (r_{xy} and r_{yy}) can be

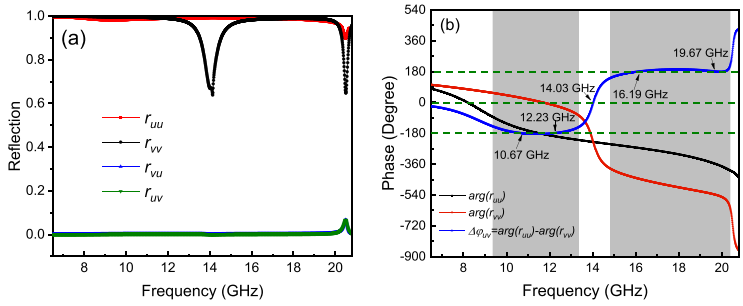

Fig. 4. (a) Simulated reflected amplitudes of the cross-polarization (r_{uv} and r_{vu}) and the co-polarization (r_{uu} and r_{vv}), and (b) phase and phase difference of the co-polarization in the u- and v-axis directions.

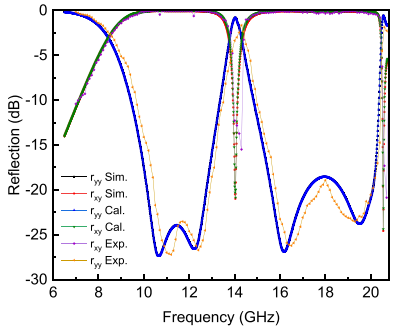

Fig. 5. Comparison of experiment, calculation, and simulation results.

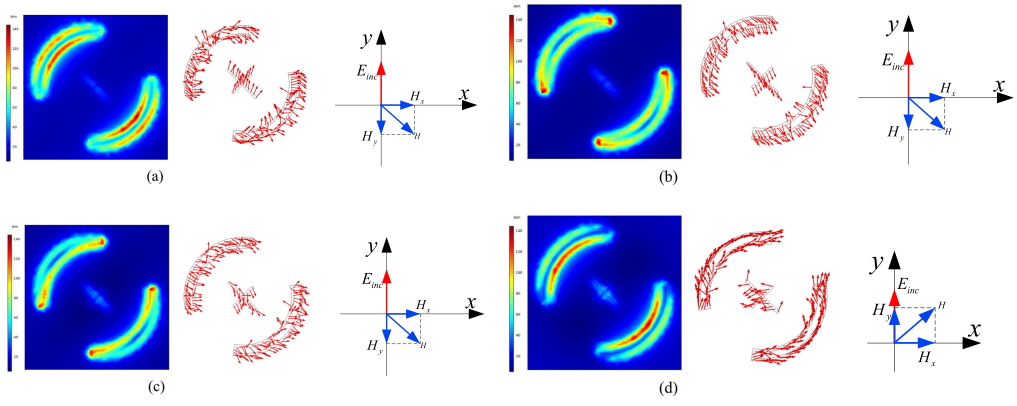

Fig. 6. The induced magnetic field distributions at the different resonance frequencies: (a) 10.67 GHz; (b) 12.22 GHz; (c) 16.18 GHz; (d) 19.51 GHz.

calculated by using Eqs. (11) and (12) and combining the phase difference $\Delta\phi_{uv}$ in Fig. 4(b). Fig. 5 shows the results of calculation, simulation and experiment. The three results agree well with each other in the case of y-polarized incident waves.

On the basis of the above analysis, it can be seen that the anisotropic structure makes r_u and r_v independent of each other, which determines the total reflection characteristics of the metasurface. The phase difference between r_u and r_v affects the reflection coefficients of the cross-polarization and the co-polarization under arbitrary polarization incidence. When the phase difference $\Delta\phi_{uv}$ is $\pm\pi$, $x(y)$ polarization is converted to $y(x)$ polarization in the two broad frequency bands.

To further understand the mechanism of the proposed polarization conversion, the induced magnetic field distributions at the different resonance frequencies under the y-polarized normal incidence are shown in Fig. 6. In Fig. 6(b), the induced magnetic field $\vec{H}$ is along the lower right

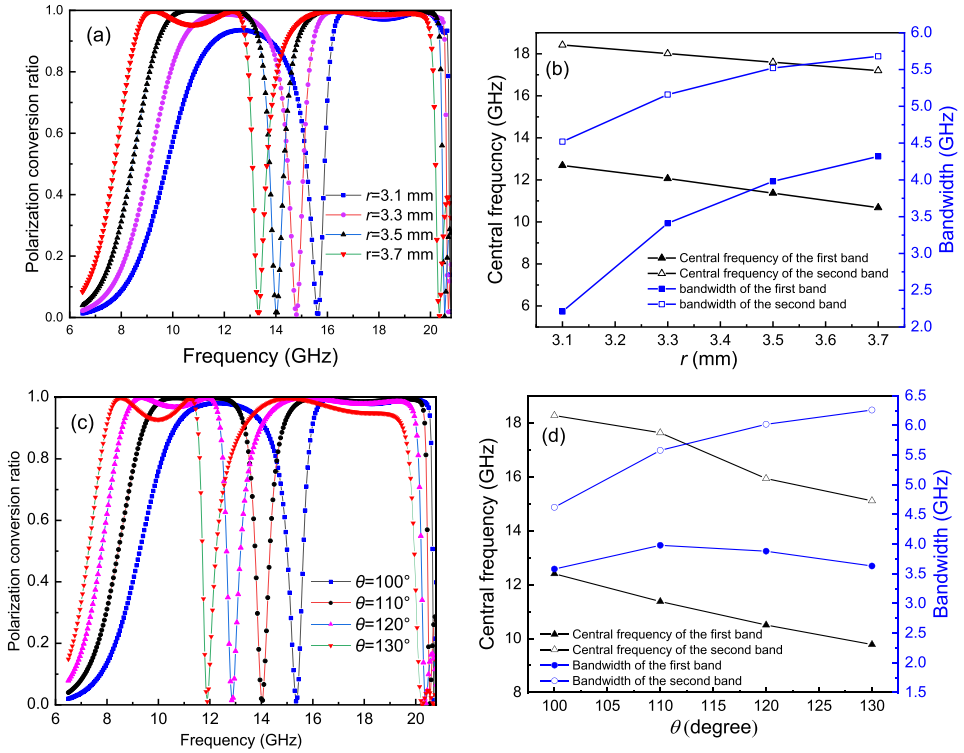

Fig. 7. (a) and (c) PCRs with various values of r and θ, respectively, (b) and (d) the central frequencies and bandwidths of the two bands corresponding to different values of r and θ, respectively.

direction at the resonance frequency of 12.22 GHz. The magnetic field $\vec{H}$ can be decomposed into two mutually perpendicular components $\vec{H}_x$ and $\vec{H}_y$, respectively. The component $\vec{H}_x$ is perpendicular to the incident electric field $\vec{E}_{inc}$. Then $\vec{H}_x$ can not generate any cross polarization conversion. The component $\vec{H}_y$, being aligned with the direction of the incident electric field $\vec{E}_{inc}$, can induce electric field that is perpendicular to $\vec{E}_{inc}$. Therefore, cross polarization conversion gets induced. The same physical mechanism is applicable for the resonant frequencies of 10.67, 16.18 and 19.51 GHz. The magnetic field component aligned with the incident electric field contributes to the polarization conversion.

4. Polarization Conversion Properties for Various Parameters

4.1 Influence of Structural Parameters

Fig. 7 shows the relationship between the structure parameters r and θ and the performance of the proposed polarization converter. As shown in Fig. 7(b), the central frequencies reduce gradually and the bandwidths increase with increasing r in the two bands. The central frequencies of the two bands red-shift and the bandwidth in the first band increases at earlier stage and decreases at latter stage, while the bandwidth in the second band increases gradually with increasing θ value, as shown in Fig. 7(d). Hence, it can be concluded that the structure parameters can adjust the performance of the designed polarization converter. As shown in Fig. 7(b), when r increases from 3.1 to 3.7 mm, the central frequency in the first band can be adjusted between 12.69 and 10.68 GHz and the corresponding relative bandwidth is 17.42–40.45%. Moreover, in the second band, the adjustment range of the central frequency is from 18.42 to 17.2 GHz and the relative bandwidth in the corresponding band is 24.54–33.02%. When θ increases from 100° to 130°, the control

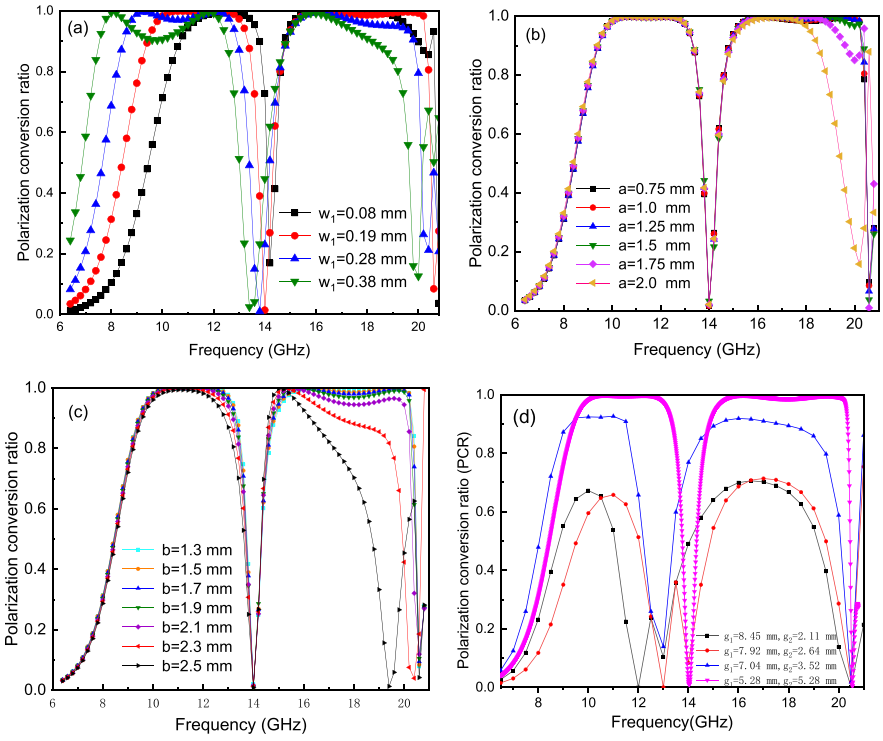

Fig. 8. PCR with different values of (a) w_1, (b) a, (c) b and (d) g_1 and g_2.

range of central frequency in the first band is 12.41 to 9.78 GHz and the related relative bandwidth is 28.87–37.14%. The central frequency in the second band ranges from 18.27 to 15.11 GHz and the relative bandwidth is 25.29–38.12%. The PCR maintains more than 95% in the whole regulation range. Therefore, the proposed polarization converter with high polarization conversion efficiency can be achieved in a wide range, implying high flexibility and selectivity of controlling the polarization state of electromagnetic waves.

In order to obtain better polarization conversion performance, the structural parameters w_1, a, b, g_1 and g_2 of the metasurface are also studied, as depicted in Fig. 8. For determining the optimal parameters, both high PCR and wide bandwidth are considered. It is seen from Fig. 8(a) that the bandwidth redshifts and become wide slightly in the first band, and the working bandwidth of the second band is narrowed gradually as w_1 increases. The PCR in the two bands decreases with increasing w_1. The bandwidth in the first band is the narrowest for $w_1 = 0.08$ mm, while the bandwidth in the second band is the widest, and the PCR is higher. For $w_1 = 0.38$ mm, the opposite result can be obtained. Therefore, $w_1 = 0.19$ mm is the best parameter simultaneously considering high PCR and wide bandwidth. Fig. 8(b) shows the PCR curves for various a values increasing from 0.75 to 1.5 mm. The bandwidths and PCR in the first band are almost unchanged. In the second band, the bandwidths and PCR gradually decrease with increasing a, and the optimal value is 1.0 mm. In addition, the value of structural parameter b varies from 1.3 to 2.5 mm and the step length is 0.2 mm. As shown in Fig. 8(c), the PCR and bandwidths decrease gradually in the first band, while the PCR and bandwidth decrease remarkably in the second band, exhibiting that the optimal value of b is 1.5 mm. However, compared with the results shown Fig. 8(b), bandwidth tends to become narrow significantly, and the decline rate of PCR is very fast, which means that b is a critical ingredient in PCR. Furthermore, the PCR as a function of the gap between two arcs is simulated, as shown in Fig. 8(d). It can be seen that the PCR and bandwidth increase remarkably as the value of g_1 decreases and g_2 increases. For $g_1 = g_2 = 5.28$ mm, the PCR is close to 1 and the bandwidth is widest in the two working bands. From the above analysis, it can be seen that the

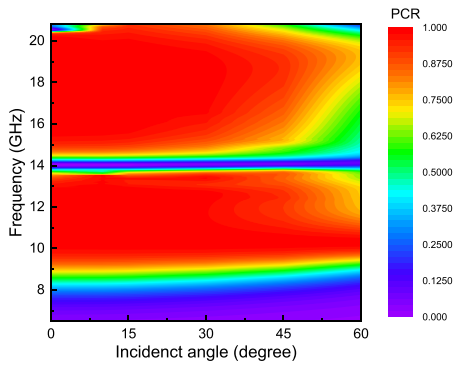

Fig. 9. Simulation results of PCRs with different incident angles.

structural parameters r, θ, w_1 g_1 and g_2 have a great impact on both low-band and high-band PCR. In addition, the structural parameters a and b have little effect on low-frequency, but have a great influence on the high-frequency band PCR. The results show that the polarization converter can be dynamically adjusted by optimizing the structure parameters.

4.2 Dependence of PCR on Incident Angle

It is expected that the reflective polarization converter possesses excellent performances at various incident angles rather than only at normal incidence. The relationship between polarization conversion efficiency and incident angle is important to polarization converter. When incident angle varies from 0° to 60°, the PCR amplitudes and resonance frequencies of the designed polarization converter are shown in Fig. 9. The simulation results show that there is almost no significant change in the PCR and working bandwidth when the incident angle increases from 0° to 45°, indicating that the polarization converter possesses good robustness and is not affected by oblique incidence. In addition, when the incident angle is 60°, the PCR reduces obviously. The reduction of PCR in the second band (14.84–20.36 GHz) is larger than that in the first band (9.38–13.36 GHz), indicating that high frequency band is more sensitive to the change of incident angle.

5. Conclusion

In summary, a broadband and high-efficient linearly polarized converter based on anisotropic metasurface is theoretically proposed and experimentally verified. Simulation results indicate that the designed metasurface can transform x- or y-polarized incident waves into their mutually perpendicular counterparts in the frequency ranges of 9.38–13.36 GHz and 14.84–20.36 GHz, and the corresponding PCR values are greater than 98.21% and 99.32%, respectively. The high-efficiency and dual-broadband characteristics are well maintained when the oblique incidence angle is up to 45°. The simulation results are consistent with the theoretical and measured results. The dual-broadband polarization conversion can also be realized by varying the geometric parameters of the structure unit in the microwave bands, exhibiting a great potential in high-efficient polarization control devices.

References

[1] H. X. Xu *et al.*, "Chirality-assisted high-efficiency metasurfaces with independent control of phase, amplitude, and polarization," *Adv. Opt. Mater.*, vol. 7, no. 4, 2019, Art. no. 1801479.
[2] C. Pfeiffer and A. Grbic, "Bianisotropic metasurfaces for optimal polarization control: analysis and synthesis," *Phys. Rev. A*, vol. 2, no. 4, 2014, Art. no. 044001/1.

[3] Y. Z. Cheng, R. Z. Gong, and Z. Z. Cheng, "A photoexcited broadband switchable metamaterial absorber with polarization-insensitive and wide-angle absorption for terahertz waves," *Opt. Commun.*, vol. 361, pp. 41–46, 2016.
[4] Y. Li, Q.S. Cao, and Y. Wang, "A wideband multifunctional multi-layer switchable linear polarization metasurface," *IEEE Antenn. Wirel. Pr.*, vol. 17, pp. 1314–1318, Jul. 2018.
[5] Y. Z. Cheng, R. Z. Gong, and J. C. Zhao, "A photoexcited switchable perfect metamaterial absorber/reflector with polarization-independent and wide-angle for terahertz waves," *Opt. Mater.*, vol. 62, pp. 28–33, 2016.
[6] X. B. Liu, "An analytical design of cross polarization converter based on the gangbuster metasurface," *IEEE Antenn. Wirel. Pr.*, vol. 16, vol. 1-1, pp. 1028–1031, 2017.
[7] O. Z. Akgol, E. Unal, O. Altintas, M. Karaaslan, F. Karadag, and C. Sabah, "Design of metasurface polarization converter from linearly polarized signal to circularly polarized signal," *Optik*, vol. 161, pp. 12–19, 2018.
[8] S. Y. Chang, X. X. Guo, and X. J. Ni, "Optical metasurfaces: progress and applications," *Annu. Rev. Mater. Res.*, vol. 48, no. 1, pp. 070616–124220, 2018.
[9] Y. Cheng, C. Wu, Z. Z. Cheng, and R. Z. Gong, "Ultra-compact multi-band chiral metamaterial circular polarizer based on triple twisted split-ring resonator," *Prog. Electromagn. Res.*, vol. 155, pp. 105–113, 2016.
[10] Y. Z. Cheng *et al.*, "Ultra broadband reflective polarization convertor for terahertz waves," *Appl. Phys. Lett.*, vol. 105, no. 18, pp. 181111–181115, 2014.
[11] A. F. Dincer, M. Karaaslan, E. Unal, O. Akgol, and C. Sabah, "Chiral metamaterial structures with strong optical activity and their applications," *Opt. Eng.*, vol. 53, no. 10, pp. 107101–107108, 2014.
[12] L. Zhang, P. Zhou, H. Chen, H. Lu, J. Xie, and L. Deng, "Adjustable wideband reflective converter based on cut-wire metasurface," *J. Opt.*, vol. 17, no. 10, pp. 105105–105112, 2015.
[13] J. Li *et al.*, "Efficient polarization beam splitter based on all-dielectric metasurface in visible region," *Nanoscale Res. Let.*, vol. 14, no. 1, 2019.
[14] Y. W. Huang *et al.*, "Aluminum plasmonic multicolor meta-hologram," *Nano Lett.*, vol. 15, no. 5, pp. 3122–3127, 2015.
[15] M. Khorasaninejad *et al.*, "Achromatic metasurface lens at telecommunication wavelengths," *Nano Lett.*, vol. 15, no. 8, pp. 5358–5362, 2015.
[16] N. Meinzer, W. L. Barnes, and I. R. Hooper, "Plasmonic meta-atoms and metasurfaces," *Nat. Photon.*, vol. 8, no. 12, pp. 889–898, 2014.
[17] L. Yang *et al.*, "High-efficiency all-dielectric transmission metasurface for linearly polarized light in the visible region," *Photon. Res.*, vol. 6, no. 6, pp. 517–526, 2018.
[18] M. Jia, Z. Wang, H. Li, X. Wang, W. Luo, and S. Sun, "Efficient manipulations of circularly polarized terahertz waves with transmissive metasurfaces," *Light-Sci. Appl.*, vol. 8, no. 1, pp. 16–28, 2019.
[19] H. X. Xu *et al.*, "Multifunctional microstrip array combining a linear polarizer and focusing metasurface," *IEEE Trans. Antennas Propag.*, vol. 64, no. 8, pp. 3676–3682, Aug. 2016.
[20] H. X. Xu, G. M. Wang, M. Q. Qi, T. Cai, and T. J. Cui, "Compact dual-band circular polarizer using twisted hilbert-shaped chiral metamaterial," *Opt. Express*, vol. 21, no. 21, pp. 24912–24921, 2013.
[21] B. Lin *et al.*, "Design of a wideband transmissive linear-to-circular polarization converter based on a metasurface," *Appl. Phys. A*, vol. 124, no. 10, pp. 715–724, 2018.
[22] B. Q. Lin, J. X. Guo, P. Chu, W. J. Huo, Z. Xing, and B. G. Huang, "Multiple-band linear-polarization conversion and circular polarization in reflection mode using a symmetric anisotropic metasurface," *Phys. Rev. Appl.*, vol. 9, no. 2, pp. 024038–024047, 2018.
[23] D. H. Kwon, G. Ptitcyn, D. R. Ana, and S. A. Tretyakov, "Transmission magnitude and phase control for polarization-preserving reflectionless metasurfaces," *Phys. Rev. Appl.*, vol. 9, no. 3, pp. 034005–034016, 2018.
[24] M. J. Moghadam, M. Akbari, F. Samadi, and A. R. Sebak, "Wideband cross polarization rotation based on reflective anisotropic surfaces," *IEEE Access*, vol. 1-1, 2018.
[25] M. Chen *et al.*, "Wideband tunable cross polarization converter based on a graphene metasurface with a hollow-carved "H" array," *IEEE Photonics J.*, vol. 9, no. 5, 2017, Art. no. 4601011.
[26] J. Hao, Y. Yuan, L. Ran, T. Jiang, and L. Zhou, "Manipulating electromagnetic wave polarizations by anisotropic metamaterials," *Phys. Rev. Lett.*, vol. 99, no. 6, pp. 063908–063912, 2007.
[27] H. Sun, C. Gu, X. Chen, Z. Li, and F. Martin, "Ultra-wideband and broad-angle linear polarization conversion metasurface," *J. Appl. Phys.*, vol. 121, no. 17, pp. 1304–1404, 2017.
[28] Y. Jia, Y. Liu, W. Zhang, and S. Gong, "Ultra-wideband and highefficiency polarization rotator based on metasurface," *Appl. Phys. Lett.*, vol. 109, no. 5, 2016, Art. no. 051901.
[29] H.Y. Chen *et al.*, "Ultra-wideband polarization conversion metasurfaces based on multiple plasmon resonances," *J. Appl. Phys.*, vol. 115, 2014, Art. no. 154504.
[30] Y. Liu, K. Li, Y. Jia, Y. Hao, S. X. Gong, and Y. J. Guo, "Wideband RCS reduction of a slot array antenna using polarization conversion metasurfaces," *IEEE Trans. Antennas Propag.*, vol. 64, no. 1, pp. 326–331, Jan. 2016.
[31] B. Q. Lin, J. X. Guo, B. G. Huang, L. B. Fang, P. Chu, and X. W. Liu, "Wideband linear-to-circular polarization conversion realized by a transmissive anisotropic metasurface," *Chin. Phys. B*, vol. 27, no. 5, 2018, Art. no. 054204.
[32] N. K. Grady *et al.*, "Terahertz metamaterials for linear polarization conversion and anomalous refraction," *Science*, vol. 340, pp. 1304–1307, 2013.
[33] D. Yang, H. Lin, and X. Huang, "Dual broadband metamaterial polarization converter in microwave regime," *Prog. Electromagn. Res. Lett.*, vol. 61, pp. 71–76, 2016.
[34] B.Q. Lin *et al.*, "Dual-band high-efficiency polarization converter using an anisotropic metasurface," *J. Appl. Phys.*, vol. 119, no. 18, pp. 183103–183112, 2016.
[35] H. Shi, J. Li, A. Zhang, J. Wang, and Z. Xu, "Broadband cross polarization converter using plasmon hybridizations in a ring/disk cavity," *Opt. Express*, vol. 22, no. 17, pp. 20973–20981, 2014.
[36] Y. Zhou, X. Cao, J. Gao, and S. Li, "A C/X dual-band wide-angle reflective polarization rotation metasurface," *Radio Eng.*, vol. 26, no. 3, pp. 699–704, 2017.